Beyond the Tamm-Dancoff approximation for extended systems using exact diagonalization

Tobias Sander, Emanuele Maggio, and Georg Kresse

University of Vienna, Faculty of Physics and Center for Computational Materials Science, Sensengasse 8/12,
A-1090 Vienna, Austria

Linear optical properties can be accurately calculated using the Bethe-Salpeter equation. After introducing a suitable product basis for the electron-hole pairs, the Bethe-Salpeter equation is usually recast into a complex non-Hermitian eigenvalue problem that is difficult to solve using standard eigenvalue solvers. In solid-state physics, it is therefore common practice to neglect the problematic coupling between the positive- and negative-frequency branches, reducing the problem to a Hermitian eigenvalue problem [Tamm-Dancoff approximation (TDA)]. We use time-inversion symmetry to recast the full problem into a quadratic Hermitian eigenvalue problem, which can be solved routinely using standard eigenvalue solvers even at a finite wave vector $\mathbf{q}$. This allows us to access the importance of the coupling between the positive- and negative-frequency branch for prototypical solids. As a starting point for the Bethe-Salpeter calculations, we use self-consistent Green's-function methods (GW), making the present scheme entirely *ab initio*. We calculate the optical spectra of carbon (C), silicon (Si), lithium fluoride (LiF), and the cyclic dimer Li_2F_2 and discuss why the differences between the TDA and the full solution are tiny. However, at finite momentum transfer $\mathbf{q}$, significant differences between the TDA and our exact treatment are found. The origin of these differences is explained.

I. INTRODUCTION

The study of optical properties of condensed matter and molecular systems is a field of growing interest, not least because of the emerging importance of renewable energies and the requirement to accurately predict the optical properties of novel composite materials and nanostructures. Time-dependent density functional theory (TDDFT) has certainly been the most widely used approach to date, although it is not without problems. In TDDFT, an effective two-point Dyson-like equation relates the density response function of the noninteracting Kohn-Sham system $\chi_0(\mathbf{r},\mathbf{r}',t-t')$ to the (linear) density response function of the interacting system $\chi^{\mathrm{TD}}(\mathbf{r},\mathbf{r}',t-t')$: $\chi^{\mathrm{TD}} = \chi_0 + \chi_0(v + f_{\mathrm{xc}})\chi^{\mathrm{TD}}$ [1]. The "interaction" terms are described by the Coulomb kernel v and the exchange-correlation kernel f_{xc}. Unfortunately, though, the interaction kernel does not allow for a systematic improvable expansion of the microscopic particle-particle interaction as would be the case, e.g., for Green's-function methods. Furthermore, or rather resultantly, only few two-point kernels, $f_{\mathrm{xc}}(\mathbf{r},\mathbf{r}',t-t')$, yield a satisfactory description of excitonic effects [2,3]. Among them, the most successful approximate kernels are the nanoquanta kernel [4–6], the bootstrap kernel of Sharma [7], and kernels based on the jellium with a gap [8]. The nanoquanta kernel requires one to explicitly calculate the two-electron four-orbital integrals, making it almost as expensive as the methods discussed below, whereas the latter two are yet not satisfactorily derived from first principles and fail to describe bound excitons accurately [7].

Alternative descriptions rely on the so-called Bethe-Salpeter equation (BSE). After some manipulation, the conventional Bethe-Salpeter equation—known from nuclear theory—can be cast into a Dyson-like equation,

$$P = P_0 + P_0 I P,$$

where $P(1,2,3,4)$ is the four-point time-ordered polarization propagator and I denotes the interaction kernel [9], and we use the common notation for space and time points $1 = (\mathbf{r}_1,t_1)$. This equation resembles the response equation for χ^{TD} from TDDFT, where P can be regarded to be a generalized linear density matrix response function to a nonlocal perturbation (cf. Eq. (63) in Ref. [10]).

Obviously, manipulation of such four-point quantities is much more involved than the simpler TDDFT two-point quantities. In practice, the polarization propagator $P(1,2,3,4)$ is expressed in a suitable two-orbital basis made up of all relevant combinations of electron and hole pairs. Furthermore, the electron-hole interaction kernel I is approximated by the Coulomb kernel v and a static (or, more correctly, instantaneous) screened interaction W. This static approximation is commonly applied to simplify the calculations. Inclusion of frequency-dependent kernels is possible and, e.g., important for the description of double excitations, but computationally much more demanding [11,12]. Also, it has been shown that quasiparticle (QP) renormalization effects cancel against dynamical effects in the interaction kernel [11]. Hence, neglecting dynamical effects as done throughout this work is expected to yield accurate results.

The excitation energies are determined by calculating the resolvent of the polarization propagator. This usually requires the diagonalization of a large matrix, where the matrix dimension equals the number of occupied states times the number of unoccupied states. Formally, the solution of this equation is then entirely equivalent to solving the so-called Casida equation for time-dependent DFT and time-dependent Hartree-Fock [13]. For hybrid functionals, the only difference is that in Casida's equation, the screened interaction W between electrons and holes is replaced by the Coulomb kernel v "screened" by the mixing parameter α. The mixing parameter α determines how much of the nonlocal exchange is included (in most cases, $\alpha = 1/4$).

In addition to the static approximation $W(t,t') = W \delta(t,t')$, which is exactly observed for hybrid functionals, since the Coulomb kernel there is, per construction, instantaneous, a further approximation is commonly applied. To solve the BSE/Casida equation, the response functions (be it the two-point or four-point variants) are usually Fourier transformed to frequency space, where they are symmetric, $\mathrm{Re}\,\chi(\omega) = \mathrm{Re}\,\chi(-\omega)$. In principle, terms between positive- and negative-frequency branches exist, describing the annihilation of two electron-hole pairs against each other, or the creation of two electron-hole pairs as a result of vacuum fluctuations. These diagrams and thus the interaction terms between the positive- and negative-frequency branch are often neglected, an approximation that is commonly referred to as the Tamm-Dancoff approximation [14,15]. Applying the Tamm-Dancoff approximation simplifies the computations tremendously, since the original full interaction matrix is not Hermitian and hence cannot be solved via standard "canned" eigenvalue solvers. After decoupling the positive- and negative-frequency part, however, the polarization propagator becomes a Hermitian matrix, for which the resolvent can be easily calculated. It is common practice to consider only the resonant part of the polarization propagator, and we refer to it here as the Tamm-Dancoff approximation (TDA). In the physics community, the full solution is usually determined by iterative solvers or time-evolution algorithms [16,17], whereas in quantum chemistry, it is common to square the original problem [18,19]. For solid-state problems, the equivalent path has not yet been explored, essentially because the involved matrices are complex instead of symmetric, and it is not immediately obvious how to generalize the equations used in quantum chemistry to the complex case. By employing time-inversion symmetry and mapping Bloch wave vectors $\mathbf{k}$ to $-\mathbf{k}$ in the negative-frequency branch, we circumvent this problem and show that a similar approach as in quantum chemistry can be used. This allows one to calculate all eigenvalues and eigenvectors of the two-particle problem with an effort that is only about 2–3 times larger than that for the Hermitian Tamm-Dancoff approximation. This opens a route to efficient and convenient calculations beyond Tamm-Dancoff with full access to all eigenvectors. We test the present approach for four simple systems, namely silicon (Si), carbon (C), lithium fluoride (LiF), and cyclic lithium fluoride dimer (Li_2F_2). We find essentially no (Si, C, LiF) or little (Li_2F_2) difference between the Tamm-Dancoff approximation and the full approach, except for small errors in the static dielectric constant. However, the Tamm-Dancoff approximation clearly fails in the case of finite momentum transfer, and we give evidence for silicon by calculating the macroscopic dielectric function within TDA and beyond TDA at finite $\mathbf{q}$. Before discussing the present theoretical approach in detail, we present a concise derivation of what is called the BSE/Casida equation. This includes a brief formal rederivation and introduction of the squared problem. Our results are then presented in Sec. IV. The present calculations are based on an entirely parameter-free description, in particular, the preceding GW calculations are state of the art. They are performed self-consistently in the Green's function G, using the quasiparticle (QP) GW method [20]. This allows one to access how well state-of-the-art procedures reproduce the experiment.

II. THEORY

A. Four-point two-particle propagator and Bethe-Salpeter equation

We consider a nonrelativistic N-electron system with Hilbert space $\mathcal{H}^N = \wedge^N \mathcal{H}, \mathcal{H} = L^2$ and the standard Hamiltonian $\hat{H} = \hat{H}_0 + \hat{V}$, where $\hat{H}_0$ corresponds to the sum of a kinetic term and a lattice periodic potential, whereas $\hat{V}$ denotes the Coulomb interaction. We assume Ψ_0 to be the nondegenerate ground state of $\hat{H}$ with energy E_0^N. The four-point propagator is defined [21,22] as ($\hbar$ is set to 1 throughout this paper)

$$
\begin{aligned}
& i\,G^4(\mathbf{r}_1 t_1, \mathbf{r}_2 t_2, \mathbf{r}_3 t_3, \mathbf{r}_4 t_4) \\
& = \langle \Psi_0 | \mathcal{T}[\hat{\psi}(\mathbf{r}_1 t_1)\hat{\psi}(\mathbf{r}_2 t_2)\hat{\psi}^\dagger(\mathbf{r}_4 t_4)\hat{\psi}^\dagger(\mathbf{r}_3 t_3)] | \Psi_0 \rangle, \quad (1)
\end{aligned}
$$

where $\mathcal{T}$ denotes the time-ordering operator and $\hat{\psi}^{(\dagger)}(\mathbf{r}t)$ denotes the field operators, with the time dependence induced by the Heisenberg picture. The free four-point propagator G_0^4 is defined analogously in terms of $\hat{H}_0$ and the corresponding ground state Φ_0 (again supposed to be nondegenerate). The Wick theorem [21] for the free $2n$-point Green's functions implies, for the free four-point propagator, the equality

$$
G_0^4(1,2,3,4) = G_0(1,3)G_0(2,4) - G_0(1,4)G_0(2,3), \quad (2)
$$

where $G_0(1,2)$ corresponds to the free propagator. For the full four-point propagator, one therefore usually makes the ansatz [22]

$$
\begin{aligned}
G^4(1,2,3,4) = {} & G(1,3)G(2,4) - G(1,4)G(2,3) \\
& - i \int d(5,6,7,8)\,G(1,5)G(2,6) \\
& \times \Gamma(5,6,7,8)G(7,3)G(8,4), \quad (3)
\end{aligned}
$$

where the so-called scattering amplitude Γ is implicitly defined by this ansatz. $G(1,2)$ denotes the Green's function defined by

$$
i\,G(\mathbf{r}t, \mathbf{r}'t') = \langle \Psi_0 | \mathcal{T}[\hat{\psi}(\mathbf{r}t)\hat{\psi}^\dagger(\mathbf{r}'t')] | \Psi_0 \rangle. \quad (4)
$$

A Feynman graph analysis shows that the scattering amplitude Γ is the sum over all amputated, skeleton graphs that can be put between two electron-hole pairs. If one defines a subsum I which corresponds to all graphs that are irreducible in the electron-hole channel, then one necessarily has

$$
\Gamma = I + (i)IGGI + (i)^2 IGGIGGI + \cdots,
$$

implying

$$
\begin{aligned}
\Gamma(1,2,3,4) = {} & I(1,2,3,4) + i \int d(5,6,7,8)I(1,5,3,6) \\
& \times G(6,7)G(8,5)\Gamma(7,2,8,4).
\end{aligned}
$$

This is the well-known Bethe-Salpeter equation [22].

B. Dyson-like equation for two-particle propagator

Introducing
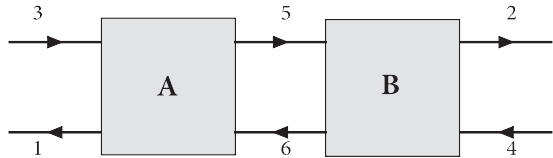
$$
L(1,2,3,4) = G^4(1,2,3,4) - G(1,3)G(2,4), \quad (5)
$$

FIG. 1. Four-point formalism for matrix multiplication: $(AB)(1,2,3,4) \stackrel{\text{def}}{=} \int d(5,6) \, A(1,5,3,6)B(6,2,5,4)$. The index order is chosen to yield a convenient order in the two-electron four orbital integrals.

one shows easily by the Bethe-Salpeter equation for Γ that L fulfills a Dyson-like equation of the form

$$L(1,2,3,4) = L_0(1,2,3,4) + i \int d(5,6,7,8)$$
$$\times L_0(1,5,3,6)I(6,7,5,8)L(8,2,7,4), \quad (6)$$

where L_0 denotes the "free part" $-G(1,4)G(2,3)$. Inherent to the above four-point matrix notation is the definition of the matrix product of four-point quantities (see Fig. 1) as

$$(AB)(1,2,3,4) \stackrel{\text{def}}{=} \int d(5,6)A(1,5,3,6)B(6,2,5,4). \quad (7)$$

As stressed in Ref. [9], the simplest contribution to the interaction kernel I, which can be written as $I = V + \tilde{I}$, is the Coulomb interaction V. All other interaction diagrams are then obtained by approximating $\tilde{I}$, which means the inclusion of certain classes of Feynman diagrams. One class of diagrams is the particle-hole ladder diagrams that includes the so-called W approximation of $\tilde{I}$, where W is the screened interaction known from Hedin's equations [23], but given in a four-point notation:

$$I(1,2,3,4) \approx V(1,2,3,4) - W(2,1,3,4), \quad (8)$$

$$V(1,2,3,4) := v(1,4^+)\delta(4,2^+)\delta(3,1^+), \quad (9)$$

$$\begin{aligned}W(1,2,3,4) &:= w(1,4^+)\delta(4,2^+)\delta(3,1^+), \\ v(1,4^+) &:= v(\mathbf{r}_1 - \mathbf{r}_4)\delta(t_1 - t_4^+), \\ w(1,4^+) &\approx \tilde{w}(\mathbf{r}_1,\mathbf{r}_4;\omega = 0)\delta(t_1 - t_4^+), \\ \delta(1,2^+) &= \delta(\mathbf{r}_1 - \mathbf{r}_2)\delta(t_1 - t_2^+).\end{aligned} \quad (10)$$

The W approximation is equivalent to the second iteration of Hedin's equations [23] with the approximation $\delta\Sigma/\delta G \approx W$ for the (irreducible) vertex function. This approximation further determines a Bethe-Salpeter equation for the irreducible polarizability (cf. Eq. (13.19c) in Ref. [23]), with W approximated in the random-phase approximation.

Notice that we assume here and in the following that both interactions are instantaneous and involve equal times $\delta(t_1 - t_4)\delta(t_4 - t_2)\delta(t_3 - t_1)$. This allows for a significant simplification. In particular, integrals of the form

$$\int d(5,6,7,8)L_0(1,5,3,6)I(6,7,5,8)L(8,2,7,4) \quad (11)$$

simplify to

$$\int dt' L_0(t_1,t',t_3,t'^+)(v - \tilde{w})L(t',t_2,t'^+,t_4), \quad (12)$$

where the spatial indices have been dropped for notational simplicity, and the interaction I possesses no frequency dependence. The crucial point is that the time limits $t_3 \to t_1^+$ and $t_4 \to t_2^+$ can now be performed under the integral, and Eq. (12) then reads

$$\int dt' L_0(t_1,t',t_1^+,t'^+)(v - \tilde{w})L(t',t_2,t'^+,t_2^+). \quad (13)$$

This suggests that two time indices suffice to solve the BSE/Casida equation, as long as the interaction is entirely static or more precisely instantaneous.

C. Polarization propagator and density fluctuation response function

The four-point propagator L is a computationally demanding object in that it depends on four arguments involving three time differences. As discussed above, the static approximation in terms of V [Eq. (9)] and W [Eq. (10)] allows one to reduce L to a quantity containing only the difference between two time arguments t_1 and t_2 and four spatial arguments. Henceforth, we will call this quantity the *time-reduced four-point polarization propagator* or density fluctuation response function $P(\mathbf{r}_1,\mathbf{r}_2,\mathbf{r}_3,\mathbf{r}_4;t_1 - t_2) = iL(\mathbf{r}_1 t_1,\mathbf{r}_2 t_2,\mathbf{r}_3 t_1^+,\mathbf{r}_4 t_2^+)$ and stick consistently with the notation of previous publications [24–26], except for a factor i. The relation to the (time-ordered) density-density fluctuation response function $\chi(1,2)$ is obtained by contraction of spatial arguments, i.e., $\mathbf{r}_3 \to \mathbf{r}_1$ and $\mathbf{r}_4 \to \mathbf{r}_2$ or, simply, $\chi(1,2) = P(1,2,1^+,2^+)$:

$$\chi(\mathbf{r}t,\mathbf{r}'t') = -i \langle \Psi_0 | \mathcal{T}[\hat{\rho}_1(\mathbf{r}t)\hat{\rho}_1(\mathbf{r}'t')] | \Psi_0 \rangle, \quad (14)$$

where the density fluctuation operator is defined as

$$\begin{aligned}\hat{\rho}_1(\mathbf{r}t) &= \hat{\psi}^\dagger(\mathbf{r}t)\hat{\psi}(\mathbf{r}t) - \langle \hat{\psi}^\dagger(\mathbf{r}t)\hat{\psi}(\mathbf{r}t) \rangle \\ &= \hat{\psi}^\dagger(\mathbf{r}t)\hat{\psi}(\mathbf{r}t) - n(\mathbf{r}),\end{aligned} \quad (15)$$

and $n(\mathbf{r})$ is the ground-state density. The relation between P and χ can be straightforwardly shown using Eqs. (1), (4), and (5).

The free four-point polarization propagator P_0 is given in the frequency domain by a Lehmann representation, which reads

$$\begin{aligned}P_0(\mathbf{r}_1,\mathbf{r}_2,\mathbf{r}_3,\mathbf{r}_4,\omega) = &\sum_{\substack{a \in \text{unocc} \\ i \in \text{occ}}} \frac{\varphi_a(\mathbf{r}_1)\varphi_i^*(\mathbf{r}_3)\varphi_i(\mathbf{r}_2)\varphi_a^*(\mathbf{r}_4)}{\omega - (\varepsilon_a - \varepsilon_i) + i\eta} \\ &+ \sum_{\substack{a \in \text{unocc} \\ i \in \text{occ}}} \frac{\varphi_i(\mathbf{r}_1)\varphi_a^*(\mathbf{r}_3)\varphi_a(\mathbf{r}_2)\varphi_i^*(\mathbf{r}_4)}{-\omega - (\varepsilon_a - \varepsilon_i) + i\eta}.\end{aligned}$$
$$(16)$$

Here and in the following, we have disregarded the spin: for the nonmagnetic case, a factor 2 must be added, whereas in the spin-polarized case, an additional sum over spins needs to be included. The set of orbitals $\{\varphi_i(\mathbf{r})\}$ constitutes an orthogonal basis and P_0 can be reformulated as

$$P_0(\mathbf{r}_1,\mathbf{r}_2,\mathbf{r}_3,\mathbf{r}_4,\omega)$$
$$= \sum_{k,l,m,n} \varphi_k(\mathbf{r}_1)\varphi_l^*(\mathbf{r}_3)\varphi_m(\mathbf{r}_2)\varphi_n^*(\mathbf{r}_4) \, P_{0ln}^{km}(\omega), \quad (17)$$

where the sum goes over all states k,l,m,n. The matrix elements $P_{0ln}^{km}(\omega)$ take the simple form

$$P_{0ln}^{km}(\omega) = \frac{n_m(1-n_k)-(1-n_m)n_k}{\omega-(\varepsilon_k-\varepsilon_m)+\mathrm{sgn}(\varepsilon_k-\varepsilon_m)i\eta}\delta_k^n\delta_l^m, \quad (18)$$

with the occupation numbers $n_{m,k} = n_i = \langle\Phi_0|\hat{n}_i|\Phi_0\rangle = \langle\Phi_0|a_i^\dagger a_i|\Phi_0\rangle$ referring to the noninteracting ground state Φ_0, i.e., $n_i = 1$ for $\varphi_i \in \{\varphi_{i_1},\ldots,\varphi_{i_N}\}$ where $\Phi_0 = 1/\sqrt{N!}\det[\varphi_{i_k}(\mathbf{r}_l)]$, and $n_{k,m} = n_a = 0$ otherwise. We use an index notation that takes into account the different transformation behavior under changes of the basis in the one-particle Hilbert space [9]. That means if one performs a change of basis in the one-particle Hilbert space given by a unitary matrix U, then the lower indices transform with U and the upper indices transform with U^*. For later purposes, we note that the matrix elements of the Coulomb potential are given (as usual) by

$$V_{kl}^{mn} = \langle mn|V|kl\rangle = \langle\varphi_m\varphi_n|V|\varphi_k\varphi_l\rangle$$
$$= \int d\mathbf{r}d\mathbf{r}'\varphi_m^*(\mathbf{r})\varphi_n^*(\mathbf{r}')v(\mathbf{r},\mathbf{r}')\varphi_k(\mathbf{r})\varphi_l(\mathbf{r}') \quad (19)$$

and the exchange terms are correspondingly defined as

$$W_{kl}^{mn} = \langle nm|W|kl\rangle = \langle\varphi_n\varphi_m|W|\varphi_k\varphi_l\rangle$$
$$= \int d\mathbf{r}d\mathbf{r}'\varphi_n^*(\mathbf{r})\varphi_m^*(\mathbf{r}')w(\mathbf{r},\mathbf{r}')\varphi_k(\mathbf{r})\varphi_l(\mathbf{r}'). \quad (20)$$

D. Solving the Bethe-Salpeter equation

According to the previous two sections, one needs to solve the Bethe-Salpeter equation for P in the frequency domain given by a Dyson-like equation [compare Eq. (6)],

$$P(\omega) = P_0(\omega) + P_0(\omega)I\,P(\omega), \quad (21)$$

where I is given by Eq. (8). It is natural to discretize the one-particle Hilbert space by restricting it to the span of the N orbitals occupied in the noninteracting reference ground state (given by a Slater determinant) and a (finite) number of M unoccupied orbitals (corresponding to excitations out of the reference ground state). This induces a discretization of the fermionic Fock space $\mathcal{F}_+(\mathcal{H})$ over $\mathcal{H}$. Correspondingly, P, V, and W turn into finite matrices in the orbital indices. In particular, $P(\omega)$ is now a frequency-dependent matrix. Before continuing, we note that the Dyson equation implies that P can be chosen to span the exact same Hilbert space as P_0, which can be shown easily by iterating the Dyson equation [Eq. (21)]. It is hence convenient to restrict the two-particle space to a subspace $\mathcal{B}$ of products of M unoccupied orbitals a, and N occupied orbitals i, $\varphi_i \otimes \varphi_a^* \in \mathcal{B}_0$ [first term in Eq. (16)] and $\varphi_a \otimes \varphi_i^* \in \mathcal{B}_0'$ [second term in Eq. (16)]. The dimension of $\mathcal{B}$ is $2MN$ and the subspace can be decomposed in terms of $\mathcal{B} = \mathcal{B}_0 \oplus \mathcal{B}_0'$ with $\dim\mathcal{B}_0 = \dim\mathcal{B}_0' = MN$. With this choice, $P(\omega)$ can be simply calculated according to

$$P(\omega) = [P_0(\omega)^{-1} - I]^{-1}. \quad (22)$$

Introducing the resonant Φ_K^{r} and antiresonant Φ_K^{a} two-orbital states (spanning $\mathcal{B}_0$ and $\mathcal{B}_0'$, respectively),

$$\Phi_K^{\mathrm{r}}(\mathbf{r},\mathbf{r}') := \varphi_i(\mathbf{r})\varphi_a^*(\mathbf{r}'),$$
$$\Phi_K^{\mathrm{a}}(\mathbf{r},\mathbf{r}') := \varphi_a(\mathbf{r})\varphi_i^*(\mathbf{r}'), \quad (23)$$

with the superindex $K = (i,a)$ ($i \in \mathrm{occ}, a \in \mathrm{unocc}$), the static interaction kernel I [cf. Eq. (8)] reduces to coupling matrix elements, where the resonant-resonant coupling reads

$$\mathcal{H}_{KJ}^{(\mathrm{r,r})} := \int d\mathbf{r}_1\ldots d\mathbf{r}_4\,\Phi_K^{\mathrm{r}}{}^*(\mathbf{r}_2,\mathbf{r}_4)I(\mathbf{r}_1,\mathbf{r}_2,\mathbf{r}_3,\mathbf{r}_4)\Phi_J^{\mathrm{r}}(\mathbf{r}_3,\mathbf{r}_1).$$

The other interactions are defined analogously. With the restriction of Eq. (8) and the definition of Eqs. (19) and (20), we can write all coupling terms in the following compact manner:

$$\mathcal{H}_{KJ}^{(\mathrm{r,r})} = \langle bi|V|ja\rangle - \langle bi|W|aj\rangle, \quad (24)$$

$$\mathcal{H}_{KJ}^{(\mathrm{a,a})} = \langle ja|V|bi\rangle - \langle ja|W|ib\rangle, \quad (25)$$

$$\mathcal{H}_{KJ}^{(\mathrm{r,a})} = \langle ji|V|ba\rangle - \langle ji|W|ab\rangle, \quad (26)$$

$$\mathcal{H}_{KJ}^{(\mathrm{a,r})} = \langle ba|V|ji\rangle - \langle ba|W|ij\rangle, \quad (27)$$

with the second superindex $J = (j,b)$ ($j \in \mathrm{occ}, b \in \mathrm{unocc}$). Using a graphical representation and considering the explicit time ordering, as commonly adopted for Goldstone diagrams, the first term in Eq. (24) describes an annihilation process [Fig. 2(a)] with the subsequent creation of a new e-h pair, whereas the second term involves the scattering process between an electron and a hole [Fig. 2(c)]. The same processes also appear in Eq. (25) and result from the complex-conjugated pair. The third coupling term [Eq. (26)] involves matrix elements of the interaction I between resonant and antiresonant two-orbital states. Here, the first term corresponds to an annihilation of an e-h pair against a conjugated h-e pair [Fig. 2(b)], and the second term describes the exchange process where the electron in the first pair annihilates against the hole in the second pair (and vice versa) [Fig. 2(d)]. The final equation describes the same process for the conjugated pairs.

The inverse of $P(\omega)$ is rewritten in a matrix form,

$$\underbrace{\begin{pmatrix} \omega\mathbb{1} & 0 \\ 0 & -\omega\mathbb{1} \end{pmatrix}}_{\omega\Delta} + \begin{pmatrix} P_0^{-1}(0) & 0 \\ 0 & P_0^{-1}(0) \end{pmatrix}$$
$$- \begin{pmatrix} \mathcal{H}^{(\mathrm{r,r})} & \mathcal{H}^{(\mathrm{r,a})} \\ \mathcal{H}^{(\mathrm{r,a})*} & \mathcal{H}^{(\mathrm{a,a})} \end{pmatrix}, \quad (28)$$

where $P_0(0)$ is the frequency-independent part of the previously defined time-reduced free four-point propagator involving only energy differences:

$$\left(P_0^{-1}\right)_J^K(0) = -(\varepsilon_a - \varepsilon_i)\delta_b^a\delta_j^i. \quad (29)$$

It is common to define the matrices A and B as

$$\begin{pmatrix} A & B \\ B^* & A^* \end{pmatrix} = \begin{pmatrix} \mathcal{H}^{(\mathrm{r,r})} & \mathcal{H}^{(\mathrm{r,a})} \\ \mathcal{H}^{(\mathrm{r,a})*} & \mathcal{H}^{(\mathrm{r,r})*} \end{pmatrix} - \begin{pmatrix} P_0^{-1}(0) & 0 \\ 0 & P_0^{-1}(0) \end{pmatrix}. \quad (30)$$

To determine $P(\omega)$ in Eq. (22), one needs to determine the poles of $P_0(\omega)^{-1} - I$, i.e., those frequencies Ω where the determinant of Eq. (28) is zero valued [27]. Hence one has to solve the resultant generalized eigenvalue problem (EVP),

$$\begin{pmatrix} A & B \\ B^* & A^* \end{pmatrix}\begin{pmatrix} X \\ Y \end{pmatrix} = \Omega\,\Delta\begin{pmatrix} X \\ Y \end{pmatrix}. \quad (31)$$
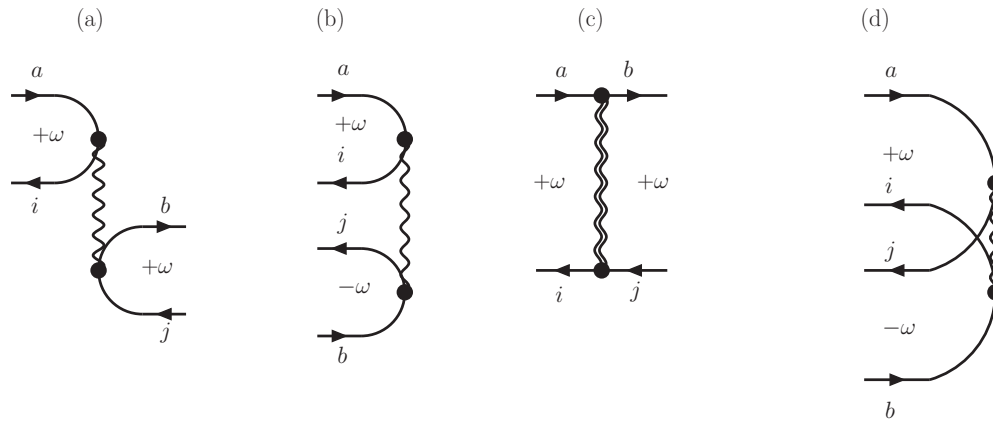
FIG. 2. Graphical representation (Goldstone diagrams) for two-particle interactions through the Coulomb potential V (wiggly line) and the static screened interaction W (double wiggly line) between electron ($\rightarrow$) and hole ($\leftarrow$), where a/b refers to unoccupied and i/j to occupied states. (a) + (c) corresponds to the resonant-resonant coupling between incoming e-h pairs (a,i) and outgoing e-h pairs (b,j). (a) The e-h pair (a,i) is destroyed at point $\mathbf{r}$, annihilating into a new pair (b,j) at point $\mathbf{r}'$. (c) Scattering process of (a,i) into (b,j). (b)+(d) describe the coupling between resonant and antiresonant e-h pairs. (b) Incoming pair (a,i) with positive frequency annihilates with pair (b,j) associated with negative frequency. (d) The e-h pair (a,i) scatters into pair (b,j) associated with negative frequency.

For real-valued orbitals in the one-particle Hilbert space, the matrices A and B are real valued and the expression can be fairly easily recast into a symmetric eigenvalue problem [18,19]. This is, however, not possible in the present case, since B and A are complex, albeit Hermitian, matrices.

As we work in a Bloch basis, we can instead proceed along the following lines. If we are interested in the response function at the wave vector $\mathbf{q} = 0$, only pairs of states $K = (i,a)$ at the same wave vectors in the Brillouin zone need to be considered, $K = (i\mathbf{k},a\mathbf{k})$. The superindex now consists of two orbital indices i and a and an additional index for the wave vector $\mathbf{k}$.

Time-inversion symmetry implies that for a Bloch eigenstate $\varphi_{n\mathbf{k}}$ of a one-particle Hamiltonian with eigenvalue $\varepsilon_n(\mathbf{k})$, the orbital $\varphi_{n,-\mathbf{k}}(\mathbf{r}) = \varphi_{n\mathbf{k}}^*(\mathbf{r})$ is also an eigenfunction with the same eigenvalue. We use this property to replace orbitals at $\mathbf{k}$ by those at $-\mathbf{k}$ in the antiresonant two-particle basis. As a first simple example, we consider the independent particle case P_0 [Eq. (16)],

$$\sum_{\substack{\mathbf{k} \\ a\in\text{unocc} \\ i\in\text{occ}}} w_{\mathbf{k}} \frac{\varphi_{a\mathbf{k}}(\mathbf{r}_1)\varphi_{i\mathbf{k}}^*(\mathbf{r}_3)\varphi_{i\mathbf{k}}(\mathbf{r}_2)\varphi_{a\mathbf{k}}^*(\mathbf{r}_4)}{\omega - (\varepsilon_{a\mathbf{k}} - \varepsilon_{i\mathbf{k}}) + i\eta}$$

$$+ \sum_{\substack{\mathbf{k}' \\ a\in\text{unocc} \\ i\in\text{occ}}} w_{\mathbf{k}'} \frac{\varphi_{i\mathbf{k}'}(\mathbf{r}_1)\varphi_{a\mathbf{k}'}^*(\mathbf{r}_3)\varphi_{a\mathbf{k}'}(\mathbf{r}_2)\varphi_{i\mathbf{k}'}^*(\mathbf{r}_4)}{-\omega - (\varepsilon_{a\mathbf{k}'} - \varepsilon_{i\mathbf{k}'}) + i\eta},$$

where $w_{\mathbf{k}}$ are $\mathbf{k}$-point weights summing to 1. By replacing $\varphi_{n,\mathbf{k}'}(\mathbf{r}) = \varphi_{n-\mathbf{k}'}^*(\mathbf{r}) = \varphi_{n\mathbf{k}}^*(\mathbf{r})$, one immediately obtains, for the antiresonant part,

$$\sum_{\substack{\mathbf{k} \\ a\in\text{unocc} \\ i\in\text{occ}}} w_{\mathbf{k}} \frac{\varphi_{i\mathbf{k}}^*(\mathbf{r}_1)\varphi_{a\mathbf{k}}(\mathbf{r}_3)\varphi_{a\mathbf{k}}^*(\mathbf{r}_2)\varphi_{i\mathbf{k}}(\mathbf{r}_4)}{-\omega - (\varepsilon_{a\mathbf{k}'} - \varepsilon_{i\mathbf{k}'}) + i\eta},$$

which is the resonant term with the position coordinates exchanged. A convenient choice, for the resonant basis and

the antiresonant basis, is therefore given by

$$\begin{aligned} \Phi_K^{\text{r}}(\mathbf{r},\mathbf{r}') &:= \varphi_{i\mathbf{k}}(\mathbf{r})\varphi_{a\mathbf{k}}^*(\mathbf{r}'), \\ \Phi_K^{\text{a}}(\mathbf{r},\mathbf{r}') &:= \varphi_{a\mathbf{k}}^*(\mathbf{r})\varphi_{i\mathbf{k}}(\mathbf{r}'). \end{aligned} \tag{32}$$

It is then easy to show that in this basis, $\mathcal{H}$ is of the form

$$\begin{pmatrix} A & B \\ B & A \end{pmatrix}, \tag{33}$$

where A and B are still Hermitian matrices. For instance, the Hartree term in the antiresonant-antiresonant block becomes (commas are introduced to separate the two bra and two ket states)

$$\begin{aligned} \mathcal{H}_{KJ}^{(\text{a},\text{a})} &= \langle j-\mathbf{k},a-\mathbf{k}'|v|b-\mathbf{k},i-\mathbf{k}'\rangle \\ &= \langle b\mathbf{k},i\mathbf{k}'|v|j\mathbf{k},a\mathbf{k}'\rangle = \mathcal{H}_{KJ}^{(\text{r},\text{r})}. \end{aligned}$$

Similar relations apply to the exchange term involving W, as well as the coupling terms between resonant and antiresonant contributions. For the Hartree term, even the antiresonant-resonant block becomes identical to the resonant-resonant block,

$$\langle j-\mathbf{k},i\mathbf{k}'|v|b-\mathbf{k},a\mathbf{k}'\rangle = \mathcal{H}_{KJ}^{(\text{r},\text{r})},$$

i.e., as in TDA, a single calculation suffices to set up all terms involving the bare Coulomb operator V, and the A and B matrices only differ by the diagonal matrix $A = B + P_0(0)^{-1}$. For the random-phase approximation (RPA) and TDDFT case, the setup of the matrices is therefore not more expensive than for TDA calculations. Only for the exchange term involving W additional matrix elements corresponding to Fig. 2(d) need to be calculated.

The solution to the generalized eigenvalue problem [Eq. (31)] can be performed by a method discussed, e.g., by Stratman *et al.* [18] and in great detail by Furche [19,28]. We summarize some aspects briefly.

Introducing a partition of the eigenvector Λ in $\mathcal{B}$ as

$$\begin{pmatrix} X_\Lambda \\ Y_\Lambda \end{pmatrix}, \tag{34}$$

where $X_\Lambda \in \mathcal{B}_0$ and $Y_\Lambda \in \mathcal{B}_0'$, the generalized EVP reads

$$\begin{pmatrix} A & B \\ B & A \end{pmatrix}\begin{pmatrix} X_\Lambda \\ Y_\Lambda \end{pmatrix} = \Omega_\Lambda \begin{pmatrix} \mathbb{1} & 0 \\ 0 & -\mathbb{1} \end{pmatrix}\begin{pmatrix} X_\Lambda \\ Y_\Lambda \end{pmatrix}. \qquad (35)$$

This is equivalent to the system of equations

$$\begin{aligned} AX_\Lambda + BY_\Lambda &= \Omega_\Lambda X_\Lambda, \\ -BX_\Lambda - AY_\Lambda &= \Omega_\Lambda Y_\Lambda, \end{aligned} \qquad (36)$$

or

$$(A - B)(X_\Lambda - Y_\Lambda) = \Omega_\Lambda(X_\Lambda + Y_\Lambda), \qquad (37)$$

$$(A + B)(X_\Lambda + Y_\Lambda) = \Omega_\Lambda(X_\Lambda - Y_\Lambda). \qquad (38)$$

From Eqs. (37) and (38), one obtains the relation

$$(A - B)(A + B)\mathbb{1}(X_\Lambda + Y_\Lambda) = \Omega_\Lambda^2 (X_\Lambda + Y_\Lambda). \qquad (39)$$

The advantage of Eq. (39) is that it is formulated in $\mathcal{B}_0$ exclusively; however, it still does not correspond to a Hermitian eigenvalue problem. This can be cured by introducing the identify $\mathbb{1} = (A - B)^{\frac{1}{2}}(A - B)^{-\frac{1}{2}}$ in Eq. (39) and defining

$$S = (A - B)^{\frac{1}{2}}(A + B)(A - B)^{\frac{1}{2}}, \qquad (40)$$

$$z_\Lambda = (A - B)^{-\frac{1}{2}}(X_\Lambda + Y_\Lambda), \qquad (41)$$

such that

$$S z_\Lambda = \Omega_\Lambda^2 z_\Lambda. \qquad (42)$$

Note that all eigenvalues come in pairs, with positive and negative frequencies $\pm\Omega_\Lambda$ corresponding to the resonant and antiresonant part of the response function. On the other hand, from Eqs. (37) and (41), it follows

$$(X_\Lambda - Y_\Lambda) = (A - B)^{-\frac{1}{2}} \Omega_\Lambda z_\Lambda. \qquad (43)$$

This equation and Eq. (41) allow one to determine X_Λ and Y_Λ. However, the "super" vector (X_Λ, Y_Λ) is not necessarily normalized [i.e., $(X_\Lambda, Y_\Lambda)\Delta(X_\Lambda, Y_\Lambda)^* \neq 1$], since the eigenvectors of Eq. (42) are only defined but for a scaling constant. Correct normalization can be achieved by multiplying each eigenvector z_Λ of the squared problem with a suitable scaling factor $z_\Lambda \to |\Omega_\Lambda|^{-\frac{1}{2}} z_\Lambda$ before solving the two linear equations [Eqs. (41) and (43)]:

$$(X_\Lambda + Y_\Lambda) = \underbrace{(A - B)^{\frac{1}{2}} |\Omega_\Lambda|^{-\frac{1}{2}}}_{C} z_\Lambda, \qquad (44)$$

$$(X_\Lambda - Y_\Lambda) = \pm \underbrace{(A - B)^{-\frac{1}{2}} |\Omega_\Lambda|^{\frac{1}{2}}}_{C'} z_\Lambda, \qquad (45)$$

where the plus sign applies to positive eigenvalues $+\Omega_\Lambda$ and the minus sign applies to the negative eigenvalues $-\Omega_\Lambda$. It is then simple to prove that [28]

$$(X_\Lambda + Y_\Lambda) \cdot (X_\Lambda - Y_\Lambda)^* = 1, \qquad (46)$$

$$X_\Lambda Y_\Lambda^* - Y_\Lambda X_\Lambda^* = 0, \qquad (47)$$

and eventually $(X_\Lambda, Y_\Lambda)\Delta(X_\Lambda, Y_\Lambda)^* = 1$, if the vectors z_Λ form an orthonormal set. The solution of the squared EVP

[Eq. (42)] yields two frequencies $\pm\Omega_\Lambda$, and the two corresponding eigenvectors $(X_\Lambda^\pm, Y_\Lambda^\pm)$ read

$$\begin{pmatrix} X_\Lambda^\pm \\ Y_\Lambda^\pm \end{pmatrix} = \frac{1}{2}\begin{pmatrix} (C \pm C')z_\Lambda \\ (C \mp C')z_\Lambda \end{pmatrix}. \qquad (48)$$

We note, however, that in most cases, it suffices to calculate $X_\Lambda^+ + Y_\Lambda^+$ as shown below for the polarizability. This sum of the eigenvectors can be trivially obtained from Eq. (44).

A few points need to be emphasized here. (i) The matrices A and B are both Hermitian. (ii) To determine $(A - B)^{1/2}$ [Eq. (42)], $(A - B)$ needs to be positive definite to make its square roots well defined and single valued. Since A and B are Hermitian, so is $(A - B)$. Furthermore, the eigenvalues of $(A - B)$ are not only real, but also positive, because positive definiteness of $(A \pm B)$ guarantees the stability of the reference state $|\Psi_0\rangle$ from which excitations are considered [28–30]. For TDDFT, if $|\Psi_0\rangle$ is the (stable) ground state, $(A \pm B)$ is positive definite and thus the excitation energies Ω_Λ are positive. Of course for GW+BSE, the positive definiteness is not guaranteed as the ground state is not determined fully consistently with the subsequent BSE calculations. However, in all cases considered here, the solutions were well defined and eigenvalues of $(A - B)$ are checked to be positive.

A final comment on the RPA and TDDFT case is appropriate here. As emphasized before, for RPA and TDDFT, the difference matrix $(A - B)$ is a simple diagonal matrix with the eigenvalue differences between the conduction- and valence-band energies in the diagonal [compare Eq. (29)]. This shows that the matrix is always positive definite, and the calculation of $(A - B)^{1/2}$ can be done at essentially no extra cost. Hence, RPA and TDDFT calculations using Casida's equation beyond TDA can be done at *no extra cost compared to TDA.*

The macroscopic dielectric function (DF) ϵ_M is finally obtained from the polarizability P [31],

$$\begin{aligned} \epsilon_M(\mathbf{q}, \omega) = 1 - \lim_{\mathbf{q}\to 0}\Big[& v(\mathbf{q})\int d\mathbf{r}_1 d\mathbf{r}_2 e^{-i\mathbf{q}(\mathbf{r}_1 - \mathbf{r}_2)} \\ & \times P(\mathbf{r}_1, \mathbf{r}_2, \mathbf{r}_1, \mathbf{r}_2, \omega)\Big]. \end{aligned} \qquad (49)$$

By exploiting the orbital representation [Eq. (17)] and the spectral representation (cf. (A18) in Ref. [28]) of $P(\omega)$, the DF [31] reads, in terms of the eigenvectors $(X_\Lambda^+, Y_\Lambda^+)$,

$$\begin{aligned} \epsilon_M(\mathbf{q}, \omega) = 1 + \lim_{\mathbf{q}\to 0} v(\mathbf{q}) \sum_\Lambda & \left(\frac{1}{\Omega_\Lambda - \omega} + \frac{1}{\Omega_\Lambda + \omega}\right) \\ \times \Bigg\{ & \sum_\mathbf{k} w_\mathbf{k} \sum_{a,i} \langle a\mathbf{k}|e^{i\mathbf{q}\cdot\mathbf{r}}|i\mathbf{k}\rangle X_\Lambda^{+(i,a)\mathbf{k}} \\ & + \langle i-\mathbf{k}|e^{i\mathbf{q}\cdot\mathbf{r}}|a-\mathbf{k}\rangle Y_\Lambda^{+(a,i)-\mathbf{k}} \Bigg\}\{c.c.\}. \end{aligned} \qquad (50)$$

Using time-inversion symmetry, the transition probabilities (term in curly brackets) simplify to

$$\sum_\mathbf{k} w_\mathbf{k} \sum_{a,i} \langle a\mathbf{k}|e^{i\mathbf{q}\cdot\mathbf{r}}|i\mathbf{k}\rangle\big[X_\Lambda^{+(i,a)\mathbf{k}} + Y_\Lambda^{+(a,i)-\mathbf{k}}\big]. \qquad (51)$$

Equation (50) assumes that the $\mathbf{q} = 0$ component of Coulomb kernel v has been set to zero, when evaluating the matrix elements of V in Eqs. (24)–(27), as discussed in detail in Ref. [31]. One can derive this result by observing that the relation between the reducible (two-point) polarizability χ and independent particle polarizability χ_0 is given by

$$\chi^{-1} = \underbrace{\chi_0^{-1} - \bar{v}}_{\bar{\chi}^{-1}} - v_0. \quad (52)$$

Here, v_0 is the (usually diverging) Coulomb kernel at the wave vector $\mathbf{q} = 0$, and $\bar{v}$ is the rest. The standard equation for the macroscopic dielectric constant is

$$\epsilon_{\mathrm{M}}^{-1} = (1 + v\chi)_{00} \quad (53)$$

$$= (1 + v_0(\bar{\chi}^{-1} - v_0)^{-1})_{00}, \quad (54)$$

where the subindex 00 implies evaluation of the matrix elements at $\mathbf{q} = 0$. Straightforward algebraic manipulation of the term after the second equation sign yields

$$\epsilon_{\mathrm{M}} = 1 - v_0\bar{\chi}, \quad (55)$$

which corresponds to Eq. (50). This equation is most likely used in most solid-state BSE codes to evaluate the dielectric constant. It is important to note that the summation is over positive- and negative-frequency branches, thus restoring the sum of the resonant and antiresonant part, even in the TDA case. Strictly speaking, such an implementation goes beyond what the TDA does (entirely neglecting one frequency branch).

E. Dielectric function at finite q vectors

For finite momentum transfer $\mathbf{q}$, the two-orbital basis reads

$$\Phi^{\mathrm{r}}_{K_{\mathbf{q}}}(\mathbf{r},\mathbf{r}') := \varphi_{i,\mathbf{k}}(\mathbf{r})\varphi^*_{a,\mathbf{k}+\mathbf{q}}(\mathbf{r}'),$$
$$\Phi^{\mathrm{a}}_{K_{\mathbf{q}}}(\mathbf{r},\mathbf{r}') := \varphi_{a,\mathbf{k}'}(\mathbf{r})\varphi^*_{i,\mathbf{k}'+\mathbf{q}}(\mathbf{r}') = \varphi^*_{a,\mathbf{k}+\mathbf{q}}(\mathbf{r})\varphi_{i,\mathbf{k}}(\mathbf{r}'), \quad (56)$$

where we have used time-inversion symmetry in the second line. With the definition given by Eq. (56), matrix elements of $\mathcal{H}$ are set up in a similar manner as in Eqs. (24)–(27). For the sake of clarity, we will show the relation for the antiresonant-antiresonant coupling pair for the Hartree kernel V. At finite momentum transfer, the resonant-resonant matrix element reads

$$\mathcal{H}^{(\mathrm{r},\mathrm{r})}_{K_{\mathbf{q}}J_{\mathbf{q}}} = \langle b\mathbf{k}+\mathbf{q},i\mathbf{k}'|v_{\mathbf{q}}|j\mathbf{k},a\mathbf{k}'+\mathbf{q}\rangle. \quad (57)$$

Replacing the momenta in the antiresonant two-orbital state $\Phi^{\mathrm{a}}_{K_{\mathbf{q}}}$ with $\mathbf{k} \to -\mathbf{k}$ and $\mathbf{k}+\mathbf{q} \to -\mathbf{k}-\mathbf{q}$, we find

$$\mathcal{H}^{(\mathrm{a},\mathrm{a})}_{K_{\mathbf{q}}J_{\mathbf{q}}} = \langle j-\mathbf{k}-\mathbf{q},a-\mathbf{k}'|v_{-\mathbf{q}}|b-\mathbf{k},i-\mathbf{k}'-\mathbf{q}\rangle$$
$$= \langle b\mathbf{k},i\mathbf{k}'+\mathbf{q}|v_{-\mathbf{q}}|j\mathbf{k}+\mathbf{q},a\mathbf{k}'\rangle$$
$$= \langle b\mathbf{k}+\mathbf{q},i\mathbf{k}'|v_{\mathbf{q}}|j\mathbf{k},a\mathbf{k}'+\mathbf{q}\rangle$$
$$= \mathcal{H}^{(\mathrm{r},\mathrm{r})}_{K_{\mathbf{q}}J_{\mathbf{q}}}.$$

The same relation also holds for matrix elements involving W, and the entire matrix $\mathcal{H}$ has the same algebraic structure as in the case of vanishing $\mathbf{q}$ vectors [Eq. (33)]. The dielectric

function is finally evaluated as

$$\epsilon_{\mathrm{M}}^{-1}(\mathbf{q},\omega) = 1 - v(\mathbf{q})\sum_{\Lambda}\left(\frac{1}{\Omega_{\Lambda} - \omega} - \frac{1}{\Omega_{\Lambda} + \omega}\right)$$

$$\times \left\{\sum_{\mathbf{k}} w_{\mathbf{k}}\sum_{a,i}\langle a\mathbf{k}+\mathbf{q}|e^{i\mathbf{q}\cdot\mathbf{r}}|i\mathbf{k}\rangle\right.$$

$$\times \left. \left(X^{+(i,a)\mathbf{k}+\mathbf{q}}_{\Lambda} + Y^{+(a,i)-\mathbf{k}-\mathbf{q}}_{\Lambda}\right)\right\}\{\mathrm{c.c.}\}. \quad (58)$$

Note that at finite $\mathbf{q}$, the full Coulomb kernel is used without disregarding any component; we thus rely on the standard expression for the macroscopic dielectric function (53). If the $q = 0$ component of Coulomb kernel v had not been set to zero in the previous section, one would have to use Eq. (58) as well (compare Eqs. (2.7) and (2.9) in [31]). The divergence of the Coulomb kernel is then canceled by the orthogonality relation between occupied and unoccupied states, and $\mathbf{k}\cdot\mathbf{p}$ perturbation theory must be used to obtain the long-wavelength contributions to the two-electron four-orbital integrals of the Coulomb kernel (for the projector augmented-wave (PAW) method, see, e.g., [32]). Our RPA-GW implementation, for instance, uses Eqs. (53) and (58) to determine the dielectric matrix, whereas the BSE code relies on the simpler-to-implement relation (50). Both yield *exactly identical results* as both relations are algebraically equivalent (compare previous section). As a matter of fact, at any momentum transfer $\mathbf{q}$, both codes (GW and BSE) yield exactly identical results for the RPA (the GW code uses two-point polarizabilities and can be applied only to the RPA).

A subtle point, however, needs to be considered. In the TDA case, Eqs. (50) and (58) are no longer equivalent, with the first equation yielding significantly more accurate results. Equation (50) disregards the coupling at all wave vectors different from $\mathbf{q} = 0$, but reintroduces the antiresonant contribution exactly in the final evaluation of the macroscopic dielectric constant; furthermore, the equation is additive in dielectric constant. Equation (58) is additive in the inverse of the dielectric constant, and if ϵ_{M} needs to be determined, it is not obvious whether the antiresonant part should be added before or after inversion. In both cases, TDA results differ from Eq. (50) as well as from the full treatment. As to why Eq. (50) is more accurate, we return to the derivation at the end of the previous section. Using (55), one first calculates $\bar{\chi}^{-1} = \chi_0^{-1} - \bar{v}$, neglecting the resonant-antiresonant coupling. However, when determining ϵ_{M}, the fully restored $\bar{\chi}$ is used, implying that the resonant-antiresonant coupling at $\mathbf{q} = 0$ is exactly accounted for. Equations (53) and (58) are fundamentally different; they include the self-consistent response of the electrons to their own field from the outset, as Eq. (52) can be rephrased as

$$\chi = \chi_0 + \chi_0 v\chi_0 + \chi_0 v\chi_0 v\chi_0 + \cdots.$$

If only the resonant part is included in χ_0, the self-consistent response to the incorrect (resonant only) part is included in the evaluation of the polarization propagator. There is no way to restore the correct response including the antiresonant part *a posteriori*. Thus, Eq. (50) is preferable to Eq. (58) and goes beyond TDA, since it correctly includes beyond-TDA contributions at $\mathbf{q} = 0$. To resolve this issue at finite $\mathbf{q}$, one

TABLE I. PAW potentials used in the present work. The columns $r_{s,p,d}$ specify the core radii for each angular quantum number in a.u. The "default" plane-wave cutoff energy $E_{\text{cut}}^{\text{pw}}$ for the orbitals is specified in eV. Column "local" specifies the chosen local potential. This is usually the all-electron potential replaced by a soft approximation inside the specified core radius.

	r_s	r_p	r_d	local	$E_{\text{cut}}^{\text{pw}}$
C	1.20	1.20	1.50	d	413
Si	1.90	1.90	1.90	d	245
Li	1.40	1.40	1.40	d	498
F	1.20	1.52	1.50	d	400

should clear the Coulomb kernel at the considered wave vector **q** and apply Eq. (50), an approach we might want to test in future work.

This line of thought also implies that many solid-state TDDFT and BSE codes yield results much superior to what the TDA should yield. It also explains why errors in the TDA are often substantial in quantum chemistry codes, which cannot easily single out the most relevant wave vector **q** = 0, and often rely on Eq. (58) to determine the response function.

III. COMPUTATIONAL METHODS

A. PAW method and potential parameters

The *ab initio* calculations presented here employ a plane-wave basis set and are performed using the VASP code [33,34]. The potentials are generated using the projector augmented-wave (PAW) method [35] to describe interactions between valence electrons and ionic cores (for details see Table I). We use the PAW implementation of Kresse and Joubert [36].

The computational procedure is the following. For each system, we perform a standard DFT calculation to obtain the Kohn-Sham orbitals and Kohn-Sham one-electron energies. The exchange-correlation part is approximated by the functional of Perdew, Burke, and Ernzerhof (PBE) [37] for silicon, whereas the local density approximation (LDA) is employed for lithium fluoride and carbon. The results are, however, independent of the starting point for the materials considered here. The subsequently calculated quasiparticle (QP) energies and orbitals are calculated within a self-consistent (sc) QP GW_0 approach [20,38,39]. The QP energies and QP orbitals are updated iteratively. The screened interaction W_0 is kept fixed at the RPA level using the original Kohn-Sham orbitals and one-electron energies. Within the sc-QP GW_0 calculations, a Hermitian eigenvalue problem is solved (cf. Eq. (3) in Ref. [39]),

$$\bar{S}^{-1/2} \bar{H} \bar{S}^{-1/2} \bar{U} = \bar{U} \bar{\Lambda}. \tag{59}$$

Initially, the QP Hamiltonian $\bar{H}$ (cf. Eq. (2) in Ref. [39]) is expressed in the basis set $\{\phi_n^{(1)}\}$, for which we use DFT orbitals. In iteration i, the solution of Eq. (59) yields the diagonal matrix $\bar{\Lambda}$ with the eigenvalues $E_n^{(i+1)}$ and the unitary matrix $\bar{U}$ holds the corresponding eigenvectors of $\bar{H}(\{E_n^{(i)}\}, \{\phi_n^{(i)}\})$. After that, the QP Hamiltonian $\bar{H}(\{E_n^{(i+1)}\}, \{\phi_n^{(i+1)}\})$ is set up with the new eigenvalues and eigenfunctions $\phi_n^{(i+1)} = \sum_m U_{mn} \phi_m^{(i)}$. The corresponding new eigenvalue problem is solved in the

TABLE II. The column $\mathcal{L}$ specifies the number of irreducible **k** points obtained from an ordinary $n \times n \times n$ **k** mesh, which is Γ centered or Monkhorst-Pack (MP) (shifted off Γ). Calculations are then performed on $\mathcal{L}$ new **k** grids ($\mathcal{M}_{p=1...\mathcal{L}}$) obtained by shifting a $m \times m \times m$ **k** grid along each irreducible **k** point $\tilde{\mathbf{k}}_{p=1...\mathcal{L}}^n$.

	k mesh	n	$\mathcal{L}$	**k** mesh ($\mathcal{M}_p$)	m
Si	Γ	3	4	Γ	16
LiF	Γ	4	8	Γ	6
C	MP	4	10	Γ	8

new basis set. This procedure is iterated until self-consistency is reached. We perform seven self-consistency steps, which gives QP energies converged to about 1 meV. After the final step, the optical matrix elements are recalculated using the final sc-QP GW_0 orbitals, and the screened Coulomb kernels W_0 are stored. In the final step, the BSE matrix is set up and the EVP given by Eq. (35) is solved.

B. Symmetry-reduced k-point meshes

To reduce the computational demand, we apply a method that was first introduced in Ref. [40]. A similar approach was later also discussed in Ref. [41].

In order to reach an accurate sampling of the Brillouin zone, we perform independent calculations for many **k**-point grids systematically shifted off Γ. The systematic shifts are calculated from a symmetry-reduced $n \times n \times n$ **k** mesh. The procedure is as follows:

(i) Generate all irreducible **k** points $\tilde{\mathbf{k}}_{p=1...\mathcal{L}}^n$ with weight $w_{p=1...\mathcal{L}}$ from a Γ-centered or Monkhorst-Pack [42] $n \times n \times n$ **k** mesh.

(ii) Generate $\mathcal{L}$, $m \times m \times m$ **k**-point grids shifted off Γ by the previously calculated shifts $\tilde{\mathbf{k}}_{p=1...\mathcal{L}}^n$; this creates $\mathcal{L}$ sets $\mathcal{M}_{p=1...\mathcal{L}}$. Calculations are performed independently for each of these sets. The results of each shifted mesh are then weighted by the previously determined weight w_p and summed up.

It is easy to see that the set $\cup_p \mathcal{M}_p$ includes all **k** points of a regular $(n \cdot m) \times (n \cdot m) \times (n \cdot m)$ **k** mesh with the proper weights. Using this trick, the computational time reduces roughly by a factor $(n^3)^2$ in the GW calculations and $(n^3)^3$ in the Bethe-Salpeter calculations, at the expense of truncating the long-range part of the Coulomb kernel at roughly m times the unit cell size. Since the exciton is well localized in LiF, m can be small for LiF without causing sizable errors, whereas larger values m are required for C and Si. The used **k**-point sets are summarized in Table II.

The dielectric functions of Si, C, and LiF shown in Figs. 3, 6, and 7 are averaged over the $\mathcal{L}$-independent calculations. The average is calculated as

$$X = \frac{1}{W} \sum_{p=1}^{\mathcal{L}} w_p X_p \quad \text{and} \quad W = \sum_{p=1}^{\mathcal{L}} w_p, \tag{60}$$

where X_p denotes the dielectric function calculated on the **k** mesh $\mathcal{M}_p$ shifted by an irreducible **k** point $\tilde{\mathbf{k}}_p^n$.
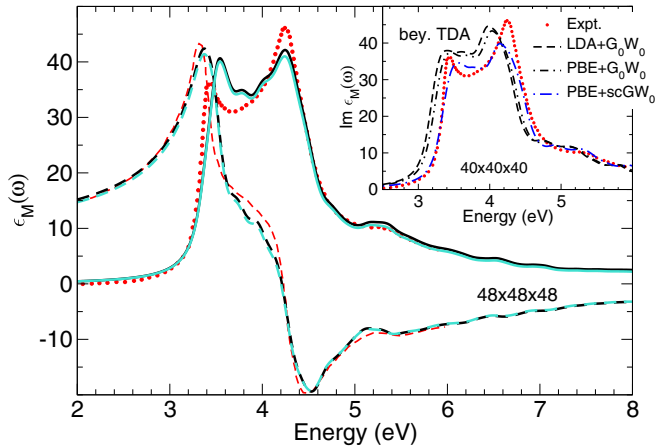
FIG. 3. (Color online) Real and imaginary part of dielectric function ϵ_M (Re ϵ_M/Im ϵ_M) of silicon predicted using sc-QP GW_0+BSE using the Tamm-Dancoff approximation (black dashed and black solid lines) and full BSE (turquoise dashed and turquoise solid lines) compared to the experimental spectrum (red dashed line and red dots) [62]. Theoretical spectra are smoothened by a Lorenzian using a complex shift of 0.1 eV. Inset: Comparison of the imaginary part of the dielectric function calculated using (i) LDA (dashed line) and PBE (double-dot-dashed line) orbitals and quasiparticle energies calculated at the G_0W_0 level, and (ii) using self-consistently iterated quasiparticle energies and orbitals (blue dot-dashed line) based on PBE orbitals and eigenvalues.

IV. RESULTS AT VANISHING MOMENTUM TRANSFER

Previous *ab initio* calculations for silicon [31,43–51], carbon [47], and lithium fluoride [49,52,53] usually included only the resonant part of the BSE-Hamiltonian. Although it is common consensus that the effects of the coupling between the resonant and antiresonant part are small [44,54–57], optical spectra explicitly including the coupling term have rarely been published [57–60].

A. Residual basis-set errors

The calculation of the frequency-dependent dielectric function [Eq. (50)] requires the summation over all possible transition pairs between occupied and unoccupied states. By imposing a cutoff for the transition states (compare Table III), high-energy excitations are neglected. This yields a residual error for the dielectric function at each frequency point. In order to estimate the total residual error for the dielectric constant (Table IV), we first calculate Re $\epsilon_M(\omega = 0)$ on a single nonshifted Γ-centered $m \times m \times m$ **k** mesh, including 12 unoccupied bands for Si, C, and LiF. This calculation is repeated now including only seven (Si) or eight (C, LiF)

TABLE III. Number of occupied and unoccupied (virtual) bands included in the calculation of the optical transition matrix elements.

	occupied	virtual
Si	4	7
LiF	4	8
C	4	8

TABLE IV. Static dielectric constant Re $\epsilon_M(\omega = 0)$ from the solution of Eq. (50) in the Tamm-Dancoff approximation (TDA) and beyond TDA. The values in parentheses are the corrected dielectric constants, where the estimated residual basis-set error is taken into account, i.e., Re $\epsilon_M(\omega = 0) + \hat{\epsilon}$ (see Sec. IV A). Experimental data are taken from Ref. [61].

Re $\epsilon_M(\omega = 0)$	Si	C	LiF
TDA	11.82 (11.87)	5.31 (5.81)	1.76 (1.96)
Beyond TDA	11.42 (11.49)	5.25 (5.65)	1.75 (1.89)
Expt.	11.90	5.70	

unoccupied bands, with four valence bands taken into account in both cases. The residual error $\hat{\epsilon}$ for the dielectric constant on this **k** mesh is the difference of both calculations, i.e., $\hat{\epsilon} =$ Re $\epsilon_M(\omega = 0; 12\,\text{CB}) -$ Re $\epsilon_M(\omega = 0; 7/8\,\text{CB})$, where CB denotes conduction bands. In Table IV, the dielectric constants are given without and with these basis-set corrections.

B. Silicon

Figure 3 shows the real and imaginary part of the dielectric function (DF) of silicon. Electron-hole pairs from the four valence bands and the lowest seven conduction bands were included to compute the dielectric function [cf. Eq. (50)]. The turquoise (solid) curve represents the results of a calculation where the full BSE-Hamiltonian is used. First of all, the present spectrum agrees very well with the experimental spectrum for the peak positions, although we have not applied any empirical shifts in the preceding quasiparticle calculations to fit the spectrum. Most notably, the position of the pronounced E_1 peak differs only by about 110 meV from experiment (at room temperature [62]) and by about 80 meV compared to measurements at 20 K [65]. The E_2 peak position agrees perfectly with the measured spectrum. According to Refs. [65,66], interband transitions exhibit a temperature dependence with respect to energy shifts and broadening [67]. In particular, the E_1 peak position is renormalized due to electron-phonon interactions. Even at zero temperature, zero-point vibrations are suggested to give rise to a shift of about 100 meV [66]. The effect of lattice vibrations has also been calculated entirely *ab initio* [51], indicating a redshift of about 80 meV for the E_1 and E_2 peaks at $T = 0$ K. This compares favorably to our calculated spectrum which does not include any phonon contributions.

The agreement for the intensities is not entirely satisfactory. In particular, the E_1 peak is slightly overestimated and the ratio of intensities (E_2/E_1) is nearly one. The present calculations correspond to an exceedingly accurate **k**-point sampling of $48 \times 48 \times 48$ points and seem to be reasonably converged with respect to the number of **k** points. However, the interaction range of the exciton is still limited by the $16 \times 16 \times 16$ subset that we used in each individual GW and BSE calculation. In fact, the spectrum is rather sensitive to the selected **k** points, as shown in Fig. 4. For instance, if the the sampling is reduced from $48 \times 48 \times 48$ to $40 \times 40 \times 40$ (and $10 \times 10 \times 10$ for the exciton interaction range), the E_1 and E_2 peaks are less pronounced. This underlines the fact that the exciton in silicon has a rather large spatial extent in real space and a dense **k**-point sampling is necessary.
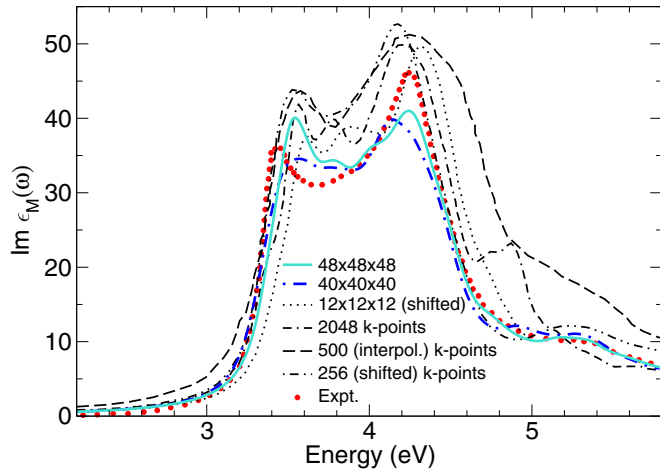
FIG. 4. (Color online) Imaginary part of the dielectric function $\epsilon_M(\omega)$ of silicon for previous calculations compared to our results (turquoise solid and blue dash-dotted lines) with regard to **k**-point sampling. In sequence of appearance in figure: (i) Ref. [63] (double-dot-dashed line), (ii) Ref. [49] (dashed line), (iii) Ref. [64] (dotted line), (iv) Ref. [44] (double-dash-dotted line). Experimental measurement (red dots) [62].

To determine how much the starting point influences the results, the inset of Fig. 3 shows a comparison of BSE calculations based on G_0W_0 calculations using either PBE or LDA orbitals. The shape of the curves agrees almost perfectly with the sc-QP GW_0+BSE calculations; however, sc-QP GW_0+BSE slightly decreases the amplitudes and shifts the spectrum to the right, thereby improving the agreement with experiment.

In Fig. 4, we compare our results with previous calculations. We suspect that the main reason for discrepancies to previous calculations are the different **k**-point sets. None of the previous calculations seems to be very well converged with respect to the number of **k** points. Some **k**-point sets enhance certain features such as the E_1 or E_2 peak. Overall, it is obvious that the present calculations match the experimental results much better than previous data.

C. Dielectric function of silicon at a finite q vector

The dielectric function at finite momentum transfer has previously been calculated mainly to investigate the dynamic structure factor [68–70] or electron energy-loss spectra [4]. However, the explicit **q** dependence of the dielectric function has been little explored [55,56], and results from the solution of the full excitonic Hamiltonian appear to have not been published.

In Fig. 5, we show the dielectric function of silicon at a finite wave vector $|\mathbf{q}| = 0.795$ a.u. along the [111] direction at different levels of approximations of the polarizability. The calculations are based on the same **k**-point grid as above, but since differences between different shifts are tiny, we have calculated the dielectric function only for a single set of shifted $16 \times 16 \times 16$ **k** points. The highest considered excitation energy was 24 eV, resulting in a BSE-Hamiltonian of roughly 200.000×200.000 if the Tamm-Dancoff approximation is not applied. Results for time-dependent DFT were previously
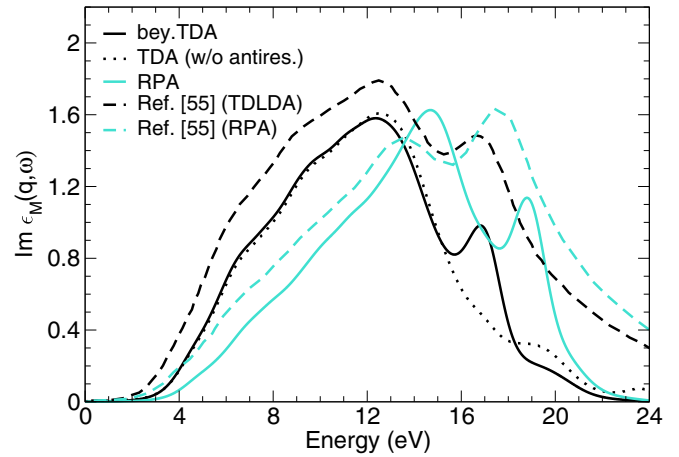

FIG. 5. (Color online) Imaginary part of the dielectric function $\epsilon_M(\mathbf{q},\omega)$ for silicon at $|\mathbf{q}| = 0.795$ a.u. along the [111] direction at the level of (i) beyond TDA (black solid line), (ii) TDA [without the negative-frequency branch in Eq. (58)] (dotted line), (iii) RPA (turquoise solid line). Reference spectra for TDLDA (black dashed line) and RPA (turquoise dashed line) are taken from Ref. [55].

published by Weissker *et al.* [55]. The important point of that study was that (i) the independent-particle (IP) approximation yields very unsatisfactory results, independent of whether the results are based on DFT or GW one-electron energies (not shown). (ii) Time-dependent DFT yields excellent agreement with experiment. On the level of the RPA, our present data are similar to the previous results, although our present calculations yield less intensity for the peak at 19 eV. The GW+BSE data follow the TDDFT and, thus, experiments well, although the amplitude is reduced compared to the TDDFT data. For the TDA, the peak around 17 eV clearly disappears, an effect that was also observed for TDDFT in Ref. [55] (Fig. 4). Note that in our TDA calculations, we have entirely neglected the antiresonant part, i.e., disregarded the negative-frequency branch in Eq. (58). The inclusion of it yields even worse agreement with the beyond-TDA spectrum. We can therefore conclude that GW+BSE describes excitonic features at zero wavelength and finite wavelength almost equally well, whereas TDDFT works well at finite momentum transfer but fails at zero wavelength, as it is not able to resolve the E_1 peak in Si.

D. Carbon

The optical spectrum of carbon is shown in Fig. 6(b). Transition energies are considered up to 36 eV including up to four valence and eight conduction bands. As before, the various characteristic positions are reproduced remarkably well, for instance the onset of absorption around 7 eV, the main peak around 12.2 eV, or the "kink" around 13 eV. However, for carbon, the peak intensity in the BSE calculations is significantly overestimated compared to the experimental values. A similar, albeit not as pronounced, overestimation was observed in a previous BSE calculation [4]. This overestimation is most likely caused by exclusion of any temperature effects on the spectrum; as shown in Ref. [51] (only for silicon), there is a gradual redshift of the peak position as well as an increase
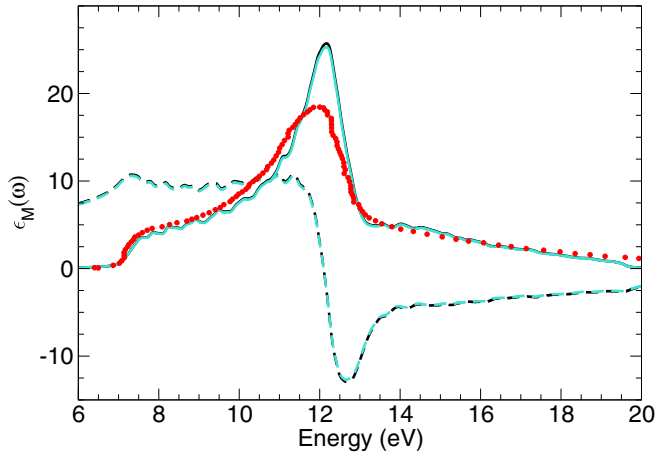
FIG. 6. (Color online) Dielectric function $\epsilon_M(\omega)$ of carbon. Color coding as in Fig. 3. Experimental spectrum (red dots) [71].

of the peak width as the temperature increases. As for Si, the difference between TDA and the full BSE is almost entirely negligible. The intensity of the main peak differs only by about 2%, so as for Si, it is safe to neglect effects beyond the TDA.

E. Lithium fluoride

The optical spectrum of LiF (Fig. 7) is obtained including the highest four valence bands and the lowest eight conduction bands. Comparison to experiment suggests again that the sc-QP GW_0+BSE yields excellent results. The first peak is slightly blueshifted compared to the experiment (about 16 meV). At first glance, the first minimum—in the experiment located around 13.6 eV—seems to be redshifted in the calculations. However, this could well be a result of the finite experimental resolution or finite-temperature broadening of the measured spectrum. As in most previous calculations, we also observe an additional sharp peak around 22.2 eV, which is absent in experiment. This peak was also present in all previous BSE calculations [4,52] and might be an artifact of either the
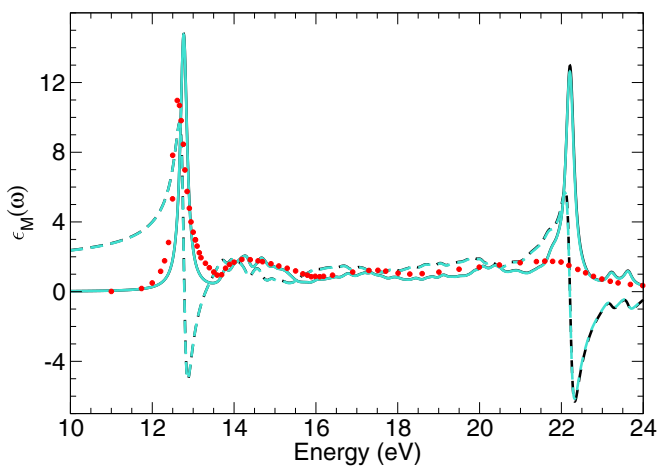

FIG. 7. (Color online) Dielectric function $\epsilon_M(\omega)$ of lithium fluoride. Color coding as in Fig. 3. Experimental spectrum (red dots) [72].
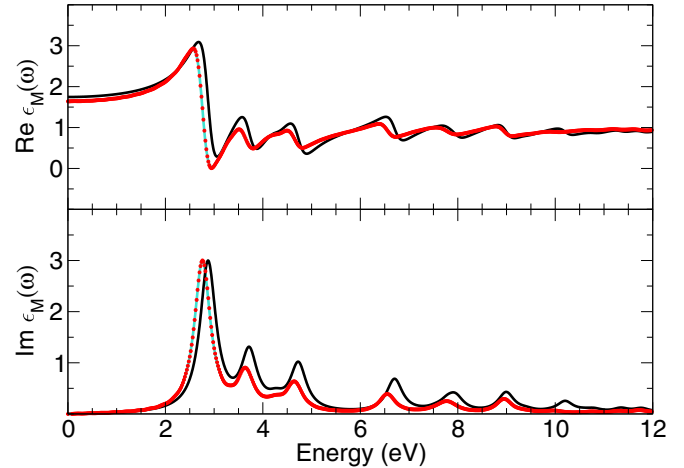

FIG. 8. (Color online) Frequency-dependent dielectric function [Re $\epsilon(\omega)$/Im $\epsilon(\omega)$] for Li_2F_2 obtained from a HF+TD-HF calculation, applying the TDA (black lines) and beyond TDA (turquoise lines). The latter ones are compared to the dielectric function obtained from a real-time propagation of the orbitals on a Hartree-Fock level (red dots). Transition pairs with an energy difference up to 16 eV are included. Structural data are taken from Ref. [76].

static W kernel or the simplified QP picture used as the starting point for the BSE calculations.

In comparison to Si and C, LiF shows almost no differences for the DF calculated within the TDA or solving the full BSE. This is in line with simple perturbation theory, which suggests that the coupling strength between the resonant and antiresonant part will be inversely proportional to the energy difference between the most prominent peaks in the resonant and antiresonant part. Therefore, as the excitation energies increase, beyond-TDA effects become less important, which is entirely in line with our observations.

F. Benchmarking the BSE code—lithium fluoride (dimer)

The previous results for the bulk systems show that solving the full excitonic BSE-Hamiltonian makes only little (Si, C) or almost no (LiF) contribution to the DF compared to the TDA at **q** = 0. However, for low-dimensional systems such as molecules, exclusion of the coupling terms of resonant/antiresonant electron-hole (e-h) pairs leads to larger errors in the optical spectrum [57]. We choose the cyclic lithium fluoride dimer (Li_2F_2) to demonstrate that the TDA is less satisfactory in describing the dielectric function of low-dimensional systems. Moreover, to give evidence that our BSE code works correctly, we compare our results obtained from time-dependent Hartree-Fock (TD-HF) calculations [on top of Hartree-Fock (HF)] against the results from a real-time propagation of the orbitals. Solving the polarizability within the TD-HF approximation requires one to solve an eigenvalue problem that is algebraically equivalent to the solution of the excitonic BSE-Hamiltonian. In the framework of TDDFT, this is known as the Casida equation [13]. Computationally, one has to calculate the same matrix elements as given in Eqs. (24)–(27). However, the screened Coulomb potential W is replaced by the bare Coulomb exchange kernel. This allows us to use the same routines to calculate the polarizability as in the case of the

excitonic BSE-Hamiltonian. On the other hand, propagating orbitals in real time for the HF-Hamiltonian allows one to calculate the polarizability for TD-HF beyond TDA without any further approximations [73–75]. We have implemented this time-propagation method in the VASP code and used it to evaluate our results for the DF beyond TDA (obtained from matrix diagonalization). The cyclic dimer Li_2F_2 shows a distinct difference between the dielectric function calculated within the TDA and beyond TDA (Fig. 8). Compared to the TDA, the entire spectrum is slightly redshifted and less pronounced at higher energies, clearly showing that coupling of resonant/antiresonant electron-hole pairs contributes to the polarizability. Similar features in the absorption spectrum have been observed for the *trans*-azobenzene molecule [57]. The overall perfect agreement of the DF using the diagonalization of the TD-HF equation and the time-propagation method confirms the correctness of the exchange terms in the beyond-TDA code.

G. Summary and conclusion

The purpose of the present paper is twofold. First we have discussed a simple and efficient method to calculate all eigenvalues and eigenvectors of the full BSE and Casida equation for solids (in the absence of spin-orbit coupling). To achieve this goal, we have replaced the orbitals at the **k** points **k** by orbitals at the **k** points $-$**k** in the antiresonant part of the BSE matrix. This approach allows one to apply methods previously used in the quantum chemistry community: the BSE can then be reformulated into a quadratic equation involving the square of the original eigenfrequencies. At the same time, the dimension of the matrix is reduced from $2N$ to N, where N is the number of particle-hole pairs. Instead of a single $2N$ non-Hermitian eigenvalue problem, now two diagonalizations of Hermitian matrices are required. This results in significant savings in computation time. All in all, the present approach is about two times more expensive than a standard Tamm-Dancoff calculation, a fairly modest computational increase. Furthermore, for time-dependent DFT, the present approach is as efficient as the Tamm-Dancoff approximation (requiring only few trivial additional calculation steps), and the required modifications of existing codes should be straightforward.

To ascertain the correctness of the implementation, we have compared the present results against a time-evolution code and found that the present approach yields exactly identical results for the Li_2F_2 dimer. Likewise, for the RPA (i.e., neglecting exchange terms), the code yields identical frequency-dependent dielectric constants as our GW-RPA implementation at **q** = 0, as well as at finite momentum transfer **q** $\neq$ 0. Compared to the time-evolution approach, the present method in combination with scaLAPACK is competitive

for matrix sizes of up to 100.000–150.000. Most importantly, it allows one to calculate all eigenvectors and eigenvalues, which is difficult for time-evolution and Lanczos algorithms that often only yield the "optical" density of states.

In the present studies, we find that the difference between TDA and beyond-TDA results is tiny in most considered simple solids. This observation is in agreement with the literature, where many authors have claimed that they have not observed any difference between TDA and beyond TDA (albeit almost always without showing the actual results). A visible change of the dielectric function is only observed for Si at finite wave vectors and for the cyclic dimer Li_2F_2. In Sec. II E, we have argued why the effects beyond TDA are so small. Our implementation, as well as all BSE implementations following Onida *et al.* [31], include beyond-TDA effects (we are not certain, though, whether all BSE codes follow this recipe). They do so by first disregarding the resonant-antiresonant coupling but at the same time disregarding the response at **q** = 0. However, in the final calculation step determining the macroscopic dielectric constants, the response at the wave vector **q** = 0 is exactly included beyond TDA. Strictly speaking, the calculated response functions go beyond the TDA. As to why this approach is less effective for molecules or larger supercells is also clear: as the cell size increases, the spacing of the reciprocal lattice vectors decreases and singling out one of the densely spaced wave vectors (e.g., **q** = 0) and treating it exactly becomes less accurate. Hence, for a molecule in a box, results are less accurate for what is commonly called the "TDA" approximation.

The second purpose of this paper is an evaluation of state-of-the-art GW+BSE calculations in comparison to experiment. To date, many BSE calculations are based on DFT orbitals and DFT one-electron energies, where the unoccupied eigenenergies are shifted to higher energies prior to the BSE calculation. Often the shift is determined by preceding GW calculations or even chosen to reproduce the peak positions in the experimental optical spectrum. Here we have instead performed self-consistent quasiparticle GW calculations (sc-QP GW_0), where the screening in W_0 was determined at the level of density functional theory and the random-phase approximation. The predicted spectra are all in excellent agreement with experiment as far as the peak positions are concerned; it is impressive how well parameter-free methods perform nowadays.

ACKNOWLEDGMENTS

---

[1] E. Gross and W. Kohn, in *Density Functional Theory of Many-Fermion Systems*, Advances in Quantum Chemistry, Vol. 21, edited by P. O. Löwdin (Academic, New York, 1990), pp. 255–291.

[2] G. Adragna, R. Del Sole, and A. Marini, Phys. Rev. B **68**, 165108 (2003).

[3] F. Bruneval, F. Sottile, V. Olevano, R. Del Sole, and L. Reining, Phys. Rev. Lett. **94**, 186402 (2005).

[4] A. Marini, R. Del Sole, and A. Rubio, Phys. Rev. Lett. **91**, 256402 (2003).

[5] L. Reining, V. Olevano, A. Rubio, and G. Onida, Phys. Rev. Lett. **88**, 066404 (2002).

[6] F. Sottile, V. Olevano, and L. Reining, Phys. Rev. Lett. **91**, 056402 (2003).

[7] S. Sharma, J. K. Dewhurst, A. Sanna, and E. K. U. Gross, Phys. Rev. Lett. **107**, 186401 (2011).

[8] P. E. Trevisanutto, A. Terentjevs, L. A. Constantin, V. Olevano, and F. D. Sala, Phys. Rev. B **87**, 205143 (2013).

[9] R. Starke and G. Kresse, Phys. Rev. B **85**, 075119 (2012).

[10] G. Csanak, H. Taylor, and R. Yaris, in *Green's Function Technique in Atomic and Molecular Physics*, Advances in Atomic and Molecular Physics, Vol. 7, edited by D. Bates and I. Esterman (Academic, New York, 1971), pp. 287–361.

[11] A. Marini and R. Del Sole, Phys. Rev. Lett. **91**, 176402 (2003).

[12] D. Sangalli, P. Romaniello, G. Onida, and A. Marini, J. Chem. Phys. **134**, 034115 (2011).

[13] M. E. Casida, in *Recent Developments and Applications of Modern Density Functional Theory*, Theoretical and Computational Chemistry, Vol. 4, edited by J. Seminario (Elsevier, New York, 1996), pp. 391–439.

[14] I. Tamm, in *Selected Papers*, edited by B. Bolotovskii, V. Frenkel, and R. Peierls (Springer, Berlin Heidelberg, 1991), pp. 157–174.

[15] S. M. Dancoff, Phys. Rev. **78**, 382 (1950).

[16] F. Fuchs, C. Rödl, A. Schleife, and F. Bechstedt, Phys. Rev. B **78**, 085103 (2008).

[17] W. G. Schmidt, S. Glutsch, P. H. Hahn, and F. Bechstedt, Phys. Rev. B **67**, 085307 (2003).

[18] R. E. Stratmann, G. E. Scuseria, and M. J. Frisch, J. Chem. Phys. **109**, 8218 (1998).

[19] F. Furche, Phys. Rev. B **64**, 195120 (2001).

[20] S. V. Faleev, M. van Schilfgaarde, and T. Kotani, Phys. Rev. Lett. **93**, 126406 (2004).

[21] K. F. H. Bruus, *Many-Body Quantum Theory in Condensed Matter Physics* (Oxford University Press, New York, 2004).

[22] G. Giuliani and G. Vignale, *Quantum Theory of the Electron Liquid* (Cambridge University Press, Cambridge, 2005).

[23] L. Hedin and S. Lundqvist, in *Solid State Physics*, Vol. 23, edited by D. T. Frederick Seitz and H. Ehrenreich (Academic, New York, 1970), pp. 1–181.

[24] L. J. Sham and T. M. Rice, Phys. Rev. **144**, 708 (1966).

[25] W. Hanke and L. J. Sham, Phys. Rev. Lett. **43**, 387 (1979).

[26] W. Hanke and L. J. Sham, Phys. Rev. B **21**, 4656 (1980).

[27] A. D. McLachlan and M. A. Ball, Rev. Mod. Phys. **36**, 844 (1964).

[28] F. Furche, J. Chem. Phys. **114**, 5982 (2001).

[29] P. Jørgensen and J. Simons, *Second Quantization-Based Methods in Quantum Chemistry* (Academic, New York, 1981).

[30] J. Čížek and J. Paldus, J. Chem. Phys. **47**, 3976 (1967).

[31] G. Onida, L. Reining, and A. Rubio, Rev. Mod. Phys. **74**, 601 (2002).

[32] M. Gajdoš, K. Hummer, G. Kresse, J. Furthmüller, and F. Bechstedt, Phys. Rev. B **73**, 045112 (2006).

[33] G. Kresse and J. Furthmüller, Comput. Mater. Sci. **6**, 15 (1996).

[34] G. Kresse and J. Furthmüller, Phys. Rev. B **54**, 11169 (1996).

[35] P. E. Blöchl, Phys. Rev. B **50**, 17953 (1994).

[36] G. Kresse and D. Joubert, Phys. Rev. B **59**, 1758 (1999).

[37] J. P. Perdew, K. Burke, and M. Ernzerhof, Phys. Rev. Lett. **77**, 3865 (1996).

[38] M. van Schilfgaarde, T. Kotani, and S. Faleev, Phys. Rev. Lett. **96**, 226402 (2006).

[39] M. Shishkin, M. Marsman, and G. Kresse, Phys. Rev. Lett. **99**, 246403 (2007).

[40] J. Paier, M. Marsman, and G. Kresse, Phys. Rev. B **78**, 121201 (2008).

[41] Y. Gillet, M. Giantomassi, and X. Gonze, Phys. Rev. B **88**, 094305 (2013).

[42] H. J. Monkhorst and J. D. Pack, Phys. Rev. B **13**, 5188 (1976).

[43] V. Olevano, S. Albrecht, and L. Reining, *Symposium B – The Optical Properties of Materials*, edited by J. R. Chelikowsky, S. G. Louie, G. Martinez, and E. L. Shirley, MRS Proceedings Vol. 579 (Materials Research Society, Pittsburg, 1999).

[44] S. Albrecht, L. Reining, R. Del Sole, and G. Onida, Phys. Rev. Lett. **80**, 4510 (1998).

[45] S. Albrecht, L. Reining, G. Onida, V. Olevano, and R. Del Sole, Phys. Rev. Lett. **83**, 3971 (1999).

[46] S. Albrecht, L. Reining, G. Onida, and R. Sole, Il Nuovo Cimento D **20**, 949 (1998).

[47] P. H. Hahn, K. Seino, W. G. Schmidt, J. Furthmüller, and F. Bechstedt, Phys. Status Solidi B **242**, 2720 (2005).

[48] Y. Ping, D. Rocca, and G. Galli, Chem. Soc. Rev. **42**, 2437 (2013).

[49] M. Rohlfing and S. G. Louie, Phys. Rev. B **62**, 4927 (2000).

[50] S. Albrecht, L. Reining, R. Del Sole, and G. Onida, Phys. Status Solidi A **170**, 189 (1998).

[51] A. Marini, Phys. Rev. Lett. **101**, 106405 (2008).

[52] L. X. Benedict, E. L. Shirley, and R. B. Bohn, Phys. Rev. Lett. **80**, 4514 (1998).

[53] M. Rohlfing and S. G. Louie, Phys. Rev. Lett. **81**, 2312 (1998).

[54] R. Zimmermann, Phys. Status Solidi B **41**, 23 (1970).

[55] H.-C. Weissker, J. Serrano, S. Huotari, F. Bruneval, F. Sottile, G. Monaco, M. Krisch, V. Olevano, and L. Reining, Phys. Rev. Lett. **97**, 237602 (2006).

[56] H.-C. Weissker, J. Serrano, S. Huotari, E. Luppi, M. Cazzaniga, F. Bruneval, F. Sottile, G. Monaco, V. Olevano, and L. Reining, Phys. Rev. B **81**, 085104 (2010).

[57] M. Grüning, A. Marini, and X. Gonze, Nano Lett. **9**, 2820 (2009).

[58] D. Rocca, M. Vörös, A. Gali, and G. Galli, J. Chem. Theory Comput. **10**, 3290 (2014).

[59] B. Baumeier, D. Andrienko, Y. Ma, and M. Rohlfing, J. Chem. Theory Comput. **8**, 997 (2012).

[60] Y. Ma, M. Rohlfing, and C. Molteni, Phys. Rev. B **80**, 241405 (2009).

[61] M. Shishkin and G. Kresse, Phys. Rev. B **75**, 235102 (2007).

[62] D. E. Aspnes and A. A. Studna, Phys. Rev. B **27**, 985 (1983).

[63] F. Sottile, K. Karlsson, L. Reining, and F. Aryasetiawan, Phys. Rev. B **68**, 205112 (2003).

[64] D. Rocca, Y. Ping, R. Gebauer, and G. Galli, Phys. Rev. B **85**, 045116 (2012).

[65] P. Lautenschlager, M. Garriga, L. Vina, and M. Cardona, Phys. Rev. B **36**, 4821 (1987).

[66] M. Cardona, Phys. Status Solidi A **188**, 1209 (2001).

[67] P. Lautenschlager, P. B. Allen, and M. Cardona, Phys. Rev. B **33**, 5501 (1986).

[68] W. A. Caliebe, J. A. Soininen, E. L. Shirley, C.-C. Kao, and K. Hämäläinen, Phys. Rev. Lett. **84**, 3907 (2000).

[69] J. A. Soininen and E. L. Shirley, Phys. Rev. B **61**, 16423 (2000).

[70] M. Gatti and F. Sottile, Phys. Rev. B **88**, 155113 (2013).

[71] H. R. Phillip and E. A. Taft, Phys. Rev. **136**, A1445 (1964).

[72] D. M. Roessler and W. C. Walker, J. Opt. Soc. Am. **57**, 835 (1967).

[73] M. Walter, H. Häkkinen, L. Lehtovaara, M. Puska, J. Enkovaara, C. Rostgaard, and J. J. Mortensen, J. Chem. Phys. **128**, 244101 (2008).

[74] K. Yabana and G. F. Bertsch, Phys. Rev. B **54**, 4484 (1996).

[75] A. Castro, M. A. L. Marques, and A. Rubio, J. Chem. Phys. **121**, 3425 (2004).

[76] F. Hampel, in *203-226: C4H10Si - S3*, The Landolt-Börnstein Database Vol. 22b, edited by P. v. Rague Schleyer (Springer, Heidelberg, 1994), p. 145.